

Interpretation of gravity and magnetic data in the Central Indian Ocean

Sistla RAVI KUMAR^{1,*} , Shaik Kareemunnisa BEGUM² 

¹ Vignan's Institute of Information Technology, Duvvada, Visakhapatnam 530046, India;
e-mail: ravikumar25450@gmail.com

² Department of Geophysics, Andhra University, Visakhapatnam- 530003, India;
e-mail: kareema-geo@yahoo.com

Abstract: The crustal deformation in the Central Indian Ocean is due to major undulations of the oceanic crust, longitudinal fracture zones, and sea-floor topography. The gravity and magnetic data along with six long profiles across the Central Indian Ocean Basin on W–E tracks between 6°S–1°S latitudes and 77°E–90°E longitudes are used to study this deformation. It has been observed that the crustal depths obtained from spectral analysis of gravity and magnetic data are in good agreement with 2D forward gravity modelling results which supports seismic results. The computed seismic velocities for the sediments are 2.0–5.7 km/s and 6.1–7.7 km/s for the oceanic igneous layer and 8.3–8.5 km/s for the oceanic upper mantle are used to determine the densities of oceanic crust with the velocity-density relationship. The average basement depths for all the gravity and magnetic profiles are obtained as ~5 km with deviations of about 1–2 km from the mean and for the deeper marker, the crustal depths vary from 9 km to 12 km. In the case of curie isotherm, the crustal depths vary from 9 km to 12 km for all magnetic profiles which may indicate deformation. The crustal top depths vary in the range of 3.5–8 km (3.2–6 km) and the bottom depth varies in the range of 8.2–13.5 km (8.5–13 km) for magnetic field anomaly data using the spectral method (the Werner method). The crustal top depths vary in the range of 3.6–6.5 km and the bottom depth varies in the range of 7.5–11.5 km for free-air anomaly data using the spectral method. The above depths are almost correlated with interpreted 2D gravity modelling and available Seismic results.

Key words: Central Indian Ocean Basin, gravity and magnetic method, deformation, tectonics, deconvolution, spectral analysis, 2D gravity model

1. Introduction

The Central Indian Ocean is considered a zone of deformation because it exhibits a large amount of intraplate seismicity (*Sykes, 1970*). The intraplate deformation and complex evolutionary history are associated with the rate

*corresponding author, e-mail: ravikumar25450@gmail.com

of spreading anomalies along the Central Indian Ridge (CIR) and southeast Indian Ridge (SEIR) as shown in Fig. 1a. The collision between the Indian and Eurasian continents is considered another major tectonic event during the Cenozoic time.

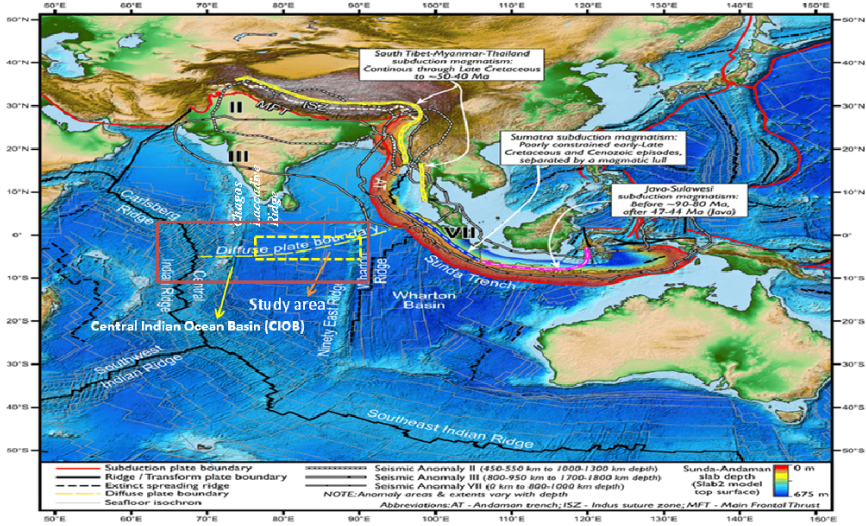


Fig. 1a. Tectonic map of the Indian Ocean, showing outlines of seismic anomalies II, III, and VII, and Late Cretaceous-Cenozoic subduction magmatism. Plate boundaries, slab-depth profile, and sea-floor isochrons were drawn from Bird (2003), Hayes et al. (2018), and Müller et al. (2019).

The tectonic map of the Indian Ocean showing plate boundaries are newly interpreted from topography, volcanism, seismicity, considering relative plate velocities from magnetic anomalies, moment tensor solutions, and geodesy (Bird, 2003) as shown in Fig. 1a. The nature of deformation and sense of faulting will be represented by the plate kinematic model (Bercovici and Wessel, 1994). Models for the mechanics of the deformation can further be compared with the principal stress directions which are inferred from focal mechanism solutions, the magnitude of the faulting, and the nature of folding. The temperature parameter is similarly important in determining the lithosphere strength (Goetze and Evans, 1979) and deformation. The brittle and elastic portion of the lithosphere strength criterion is relatively independent of temperature, but the plastic portion strongly depends on

temperature. So, the computed moment depends on the portion of the geotherm above 650°C which is at the point of transition between elastic and ductile behaviour as well as the curvature of the plate. The maximum moment is dependent on the deflection of the plate and the flexural stiffness of the plate (Goetze and Evans, 1979). The heat flow within the Central Indian Basin is about 10–40 mW/m² which is larger than expected for its age (Geller et al., 1983; Stein and Weissel, 1990).

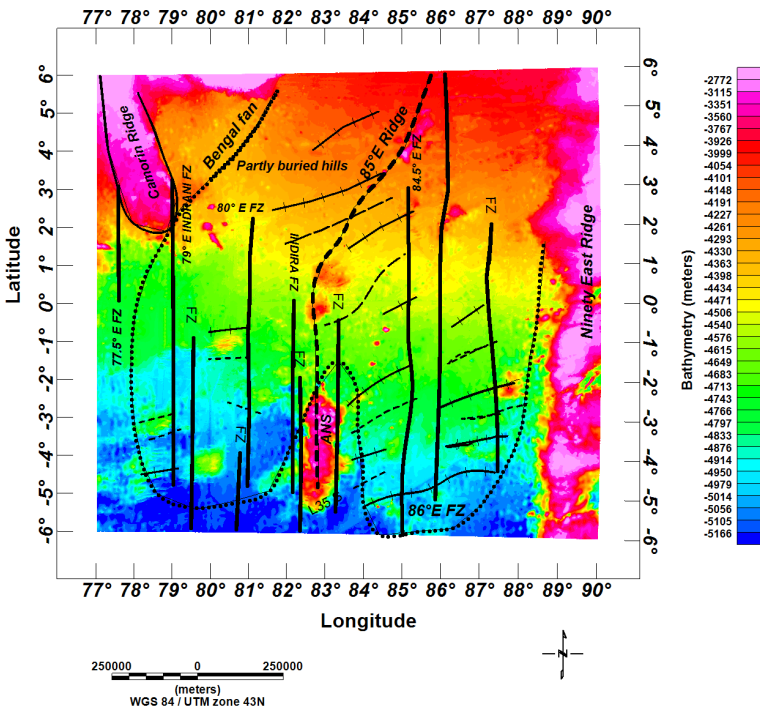


Fig. 1b. Bathymetry map of Central Indian Ocean, South of Sri Lanka showing basement undulations, crests (+++) and troughs (---) from Geller et al. (1983), major fracture zones (FZ) from Royer and Chang (1991), Wessel et al. (2015)), the limit of Bengal fan (dotted lines).

The bathymetry map and Free-air gravity map of the Central Indian Ocean Basin (CIOB) are shown in Fig. 1b, c. The deformation pattern is additionally reflected within the gravity data (Haxby, 1987), which has three prominent features within the north-eastern Indian ocean which are Ninety East, 85°E, and the Southern Chagos-Laccadive Ridges.

The deformation over this region has been explained in terms of a diffuse plate boundary between the Indian and Australian plates (*DeMets et al., 1988; Petroy and Wiens, 1989; Gordon et al., 1990; Royer and Chang, 1991*). The deformation, although dominantly compressive, also has a strike-slip component (*Bull and Scrutton, 1990; Bull et al., 1992*).

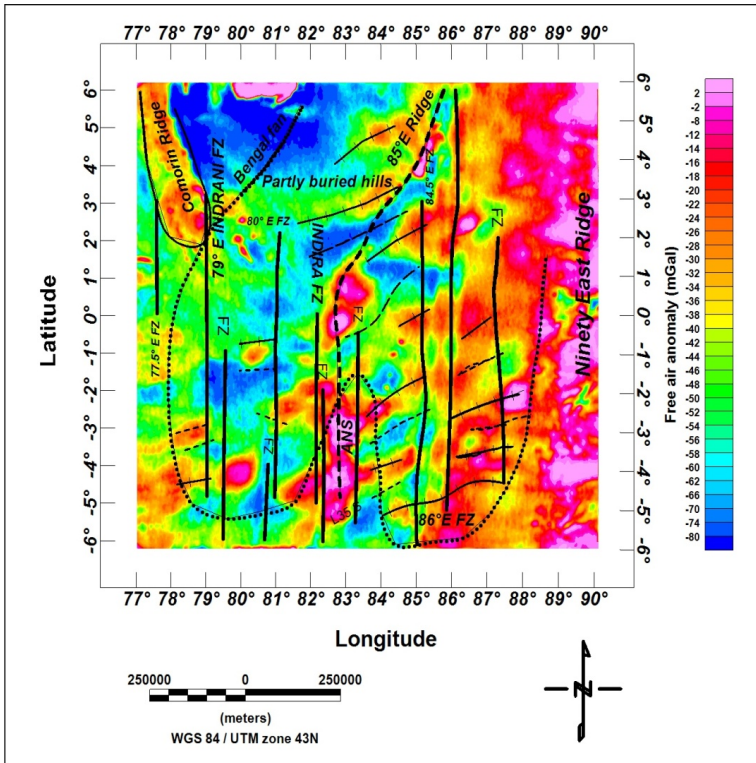


Fig. 1c. Free-air gravity map of Central Indian Ocean, South of Sri Lanka showing basement undulations, crests (+++) and troughs (---) from *Geller et al. (1983)*, major fracture zones (FZ) from *Royer and Chang (1991)*, *Wessel et al. (2015)*, the limit of Bengal fan (dotted lines).

The tectonic features like faults having different physical properties such as density or susceptibility indicate specific geological processes, so their modelling is one of the most important aspects in geological sciences (*Raju et al., 1998*). The tectonic deformation is observed as long-wavelength (100–300 km) undulation of the oceanic basement and overlying sediments and

shorter-wavelength (5–10 km) reverse faults and associated folds (buckling).

The folds related to reverse faults occur within the hanging walls of reverse faults and appear on multichannel profiles, which are restricted to the sedimentary layer (*Bull and Scrutton, 1990*). Seismic reflection studies of the CIOB deformation zone (*Krishna et al., 1998*), confirmed the existence of long-wavelength (150–300 km) anticlinal shape basement structures, with 1–2 km relief and narrow folding with high angle faulting (5–20 km long) of the oceanic basement with overlying sediments. A total of twenty-three deformed crustal blocks bounded by longitudinal fracture zones 79°E FZ, 80°E FZ, Indira FZ, 84.5°E FZ, and 86°E FZ between 77° to 88°E and 5°S to 4°N are noted from the integrated interpretation of the sea-floor topography, gravity, and seismic data (*Gopala Rao et al., 2004*). The occurrence of intense tectonic deformation was reported in CIOB as shown in Fig. 1a is based on high seismicity, unusual heat flow, gravity/geoidal anomalies, and seismic records (*Desa and Ramana, 2021; Weissel et al., 1980; Geller et al., 1983*). The characteristics of the magnetic anomaly are studied in a part of the deformation zone of the Central Indian Ocean (CIO) lying between 6°N–18°S and 76°–84°E (*Divya Bharathi et al., 2020*).

From the analysis of the bathymetry, gravity, and seismic reflection data of the diffusive zone of the CIO, an extended (~150 km) basement trough deepens by one kilometre from the regional trend (northern dipping), has been identified (*Krishna et al., 2002*). A Free-air gravity low of 20 mGal with a regional high of 8 mGal has been interpreted as due to a broad basement trough with the local rise (diapiric structure) of 10 km width. Seismic analysis (*Krishna et al., 2002*) reveals that horizontal crustal compressions within the diffusive plate boundary may be the rationale for the formation of the basement trough. However, the occurrence of deformed crustal blocks within the selected area is reported (Fig. 1c) from an integrated interpretation of longitudinal fracture zones, sea-floor topography, seismic reflection, and qualitative analysis of gravity data (*Gopala Rao et al., 2004*).

Central Indian Ocean Basin (CIOB) occurs within the middle of the Indo-Australian plate among 5°N and 10°S where deformation occurs at plate edges as shown in Fig. 1a. Seismic studies revealed an intensely deformed crust consisting of anticline structures of the upper crust and overlying sediments of the CIOB area. The earthquake focal mechanism studies in CIOB

suggest that North-South crustal deformation is because of compression and right-lateral strike-slip faults along the Ninety East Ridge (NER) (*Stein and Okal, 1978*). Recent seismic reflection studies divulge periodic deformation during Miocene (7.5–8.0 Ma), Pliocene (5.0–4.0 Ma), and Pleistocene (0.8 Ma) and intense deformation are due to closely spaced high angle faults and narrow folds. Geophysical studies depict that the deformation occurs by one among the subsequent processes (i) The plate end geodynamics and resistive forces having in-plane compression, (ii) thermo-mechanical subsidence under excess loading of igneous origin initiating lithosphere flexure under compression, and (iii) periodic deformation caused due to backward thrust from the Himalayas and plate edge geodynamics.

2. Major tectonic features of the study area

2.1. Ninety East Ridge

The Ninety East Ridge (NER) is along the north of the equator in the Eastern Indian Ocean is vigorously deforming and the ridge basement is elevated up to 2 km with corresponding Bengal Fan (*Mukhopadhyay and Krishna, 1995*). Seismic studies reveal the abundance of the ridge under sediments for 700 km north of 10°N, where the ridge is thrust under the Fan sediment (*Curray et al., 1982*). The ridge is associated with the Free-air gravity high of 50 mGal amplitude and 350 km wavelength, along with strike continuity of 1500 km in a north-south direction. The gravity analysis concludes that the ridge covers momentous crustal mass anomalies reliable with the hot spot model (*Morgan, 1983; Peirce, 1978; Duncan, 1981; Goslin and Phillippe, 1984*). The anomalous mass is very less dense by about 0.27 gcm^{-3} than the adjacent oceanic upper mantle which acts as a ‘cushion’ for the isostatic compensation mechanism of the ridge (*Mukhopadhyay and Krishna, 1995*).

The buried Ninety East Ridge as observed on seismic reflection data can be identified for another 700 km farther north to about 17°N below the Quaternary-Eocene sediments of the Bengal Fan (*Curray et al., 1982*). The NER is elevated by about two kilometres concerning the neighbouring Bengal fan oceanic crust with an average width is about 350 km along the east-west direction (*Mukhopadhyay and Krishna, 1995*). The ridge is

regarded as a Free-air ‘high’ of 50 mGal and not the same over the extent of the NER.

2.2. 85°E Ridge

The 85°E Ridge continues from the Mahanadi Basin to the Afanacy Nikitin Seamount in the Central Indian Ocean. The ridge is coupled with a negative anomaly related to the north region which is up to 5°N latitude, and the ridge is underlying the thick Bengal Fan sediments. The prominent negative gravity anomaly associated with the 85°E Ridge in the Bay of Bengal region changes to positive south of 5°N and further south, the Afanacy Nikitin Seamount is associated with a significant positive gravity anomaly (*Sreejith et al., 2011*). *Krishna (2003)* anticipated an alternative forward gravity model, in which he interpreted the negative gravity anomaly because of the density contrast between the metasediments and less dense ridge material and an extensive Moho depression beneath the ridge. The northern component of the ridge (north of 5°N) is concealed under thick Bengal Fan sediments, whereas in the south, its structure sporadically rises above the seafloor (*Curray et al., 1982; Liu et al., 1983; Curray and Munasinghe, 1991; Müller et al., 1993; Gopala Rao et al., 1997; Subrahmanyam et al., 1999; Krishna, 2003; Krishna et al., 2014*).

The gravity anomalies of the ridge were simulated for various crustal structures of existing three geological ages named Late Cretaceous, Early Miocene, and Present (*Sreejith et al., 2011*). The ridge was coupled with a significant positive anomaly during the Late Cretaceous with a compensation generated by a broad flexure of the Moho boundary. The variation of the initial gravity anomaly to the minor positive anomaly of the ridge is due to enclosing post-collision sediments by the early Miocene. At present, the ridge is underlying with three kilometres thick Bengal Fan sediments on its crustal section with pre and post-collision sediments having eight kilometres thickness on its flanks. This environmental setting had transformed the slight positive gravity anomaly into a specific negative gravity anomaly (*Sreejith et al., 2011*).

2.3. Afanacy Nikitin Seamount

The Afanacy Nikitin Seamount (ANS) joins the 85°E Ridge during isolated

buried hills and prevailing subsurface structures and together they form a linear ridge system (Krishna, 2003; Curray and Munasinghe, 1991). The gravity mark of the ridge system changes from negative to positive towards the south of 5°N , which seems to match with thinning of pre-collision continental sediments in the Bay of Bengal (Krishna, 2003). A thick pile of Bengal Fan sediments had a great impact on beneath pre-collision sediments as well as on basement rocks which the process resulted in attaining high velocities, up to 6.6 and 7.1 km/s, respectively. Gravity model studies recommend that structures of the ridge system are compensated in different modes. The ANS is underlain by an eight kilometres thick, deep crustal body of magmatic rocks, while beneath other structures oceanic crust is down-flexed up to 2.5 km (Krishna, 2003). The presence of metasediments, denser than volcanic rocks, and flexure of the lithosphere would describe the negative gravity anomaly over the 85°E Ridge (Krishna, 2003; Naini and Leyden, 1973; Curray, 1994). The lack of metasediments and magmatic rocks at depth would elucidate the compensated positive anomaly over the ANS. When the lithosphere underneath the ridge was approximately 35 million years old then the width of the 85°E Ridge, the wavelength (~ 190 km) and amplitude (~ 2.5 km) of the flexed oceanic crust, and the intersection of the ridge with the Mesozoic fracture zones suggest that the ridge was formed in intraplate position (Krishna, 2003). The hotspot forming the 85°E Ridge had reactivated the ANS during the Palaeocene and brought it to the sea surface (Krishna, 2003; Curray and Munasinghe, 1991). Then it underwent erosion and subsidence processes. The deformation activity had converged the north and south parts of the ANS in late Miocene and again in late Pleistocene and northward buried hills in early Pliocene (Krishna, 2003; Krishna et al., 1998; Krishna et al., 2001).

Crustal structures beneath the ANS buried hills, and 85°E Ridge is compensated in different modes. The crustal thickness of the ANS is ~ 18 km (Krishna et al., 2014). The seamount is compensated by flexure of the crustal layer up to the extent of ~ 1.5 km and by 8 km thick magmatic rocks in the lower crust (Krishna, 2003). Beneath buried hills and 85°E Ridge, the crust is down flexed up to 2.5 km in response to volcanic loads. North and south parts of the ANS had experienced convergence due to the deformation activity in the late Miocene (7.5–8.0 Ma) and again in the late Pleistocene (0.8 Ma), while the buried hills in the north converged in the

early Pliocene (4.0–5.0 Ma) (*Krishna, 2003*).

2.4. Indrani fracture zone

The Indrani fracture zone lies on either side of the SEIR and has its southern segment extending northward from the eastern edge of Crozet Island on the Antarctic Plate. The topography has steep gradients in the south and is gentle to the north. The seafloor along the western flank is shallower than that of the eastern flank. Seamounts surrounding this FZ are mostly situated in the southern part (*Kamesh Raju, 1993; Das et al., 2005; Das et al., 2007*). There is a noticeable difference in the morphology of seamounts that lie on either side of this FZ where smaller multi-peaked seamounts to the east and larger single-peaked ones to the west. Several east-west trending ridge parallel lineations curve toward the south at the contact with the Indrani fracture zone. The yielding of these lineations occurs mainly on the crust formed at a fast-spreading rate between 60 and 50 Ma (chron 26–23, 80 mm/year), indicative of a fast-slipping transform fault environment during its formation (*Mukhopadhyay et al., 2017*). The causative factor for such bending could have been the strong shear coupling at the contact of the FZ with the spreading ridge. The Free-air gravity values along this FZ vary from 0 to –45 mGal, with a consistently high average gravity value of 20 mGal (*Mukhopadhyay et al., 2017*). The lithospheric thickness of this fracture zone deduced from the gravitational edge effect is estimated to be around 100 km (*Mukhopadhyay et al., 2008*).

2.5. Indira fracture zone

The Indira fracture zone runs in a north-south direction along 83°E longitude and offsets the magnetic lineation from chron 34 to 20 right laterally by about 160 km (*Krishna, 2003*). The single-channel seismic profile of the southern part of this FZ indicates that the seafloor topography manifests as a discrete U-shaped graben with differing flank relief. The depth of this graben gradually increases from the neighbouring flanks to about 1700 m (*Mukhopadhyay et al., 2008*). The axial part of the graben consists of micro troughs and rises. The western flank of this FZ is shallower by 750 m and contains step-like structures. The eastern flank is deeper than the western one due to its older age. Faults exist mostly at the subsurface level al-

though some, reaching a greater depth, probably developed later than the main fracture zone (*Krishna, 1996*).

3. Data and Methodology

3.1. Data

The bathymetric data was extracted from GEBCO Grid (*GEBCO Compilation Group, 2019*), and digitized at one kilometre interval which integrates land topography and ocean bathymetry. The bathymetry varies from 2.6–5.2 km and minimum at ANS and NER as shown in Fig. 2a. The bathymetry variations depict the major tectonic features like ridges and seamounts. The sediment isopach map (*Straume et al., 2019*) of the region (Fig. 2b), shows that the thickness of sediments is decreasing towards the south. The seafloor in this region is extremely smooth with a gentle north-to-south gradient and variations in sedimentary thickness correspond to undulations in the basement topography (*Curray et al., 1982*). The sediment thickness decreases towards the eastern direction and minimum at the Ninety East Ridge.

The Free-air gravity anomaly data (Fig. 2c) is extracted from global one-minute grids (*Sandwell et al., 2014*) and digitized at a one-kilometre interval. The Free-air anomaly data contains information down to very short wavelengths (< 20 km), so it is useful in regional geophysical investigations (*Kalra et al., 2014*). The Free-air anomaly overall varies in the range of –80 to +50 mGal.

The Marine magnetic data (Fig. 2d) is extracted from global two-minute grids (*Maus et al., 2009*) and digitized at the one-kilometer interval. It was observed that the amplitude of the magnetic field anomaly varies in the range of –320 nT to 240 nT. It can be observed that the shape of the anomalies depends on the thickness and susceptibility.

A series of positive and negative magnetic anomalies in the intensity of the magnetic field is the source of permanent magnetization carried by titanomagnetite minerals in basalt and gabbros. Short wavelength and high amplitude magnetic anomalies of this region are indicative of shallow magnetic basement changes (*Rabinowitz and LaBrecque, 1977*). From the Free-air gravity and magnetic anomaly maps (Figs. 2c, d), distinct anomaly closures either elongated in NE–SW or circular are observed (*Gopala Rao et*

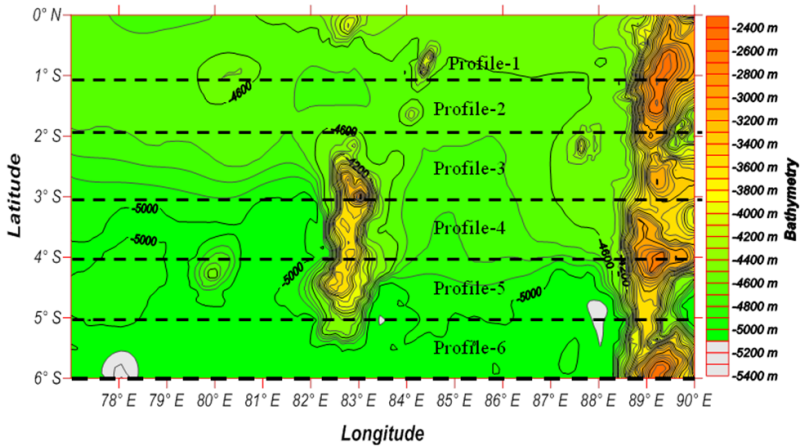


Fig. 2a. Bathymetry map of the study area. Dashed lines indicate the locations of magnetic and gravity profiles.

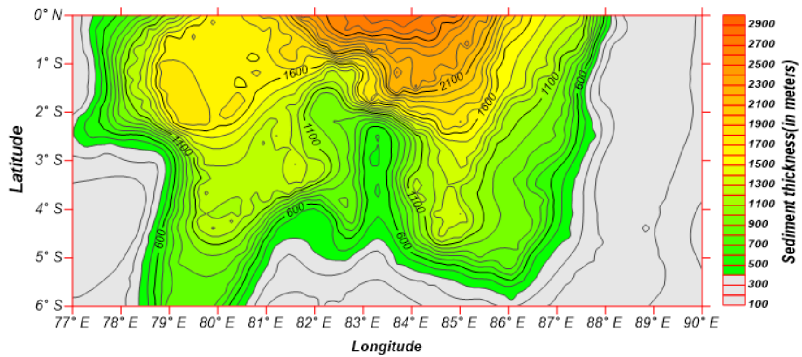


Fig. 2b. Sediment thickness map of the study area.

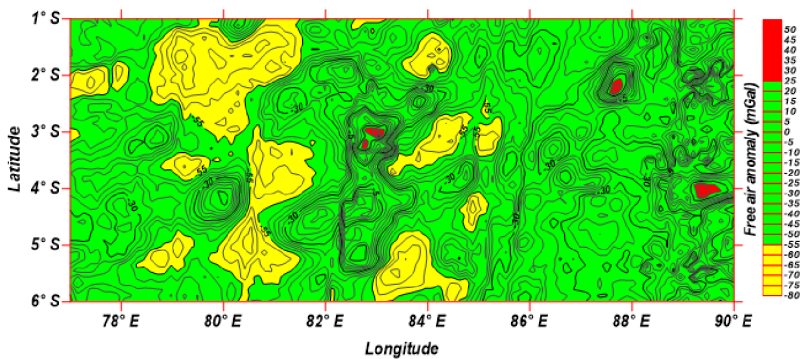


Fig. 2c. Free-air anomaly map of the study area.

al., 2004).

The areas of broad magnetic intensity anomaly closures as shown in Fig. 2d are zones of structural displacement associated with deep-seated basement, areas of magmatic intrusions, fractures, and fault zones. A comparison of EMAG2 magnetic field data with Ship track line data is shown in Fig. 2e. EMAG2 is a global 2-arc-minute high-resolution grid of the earth's

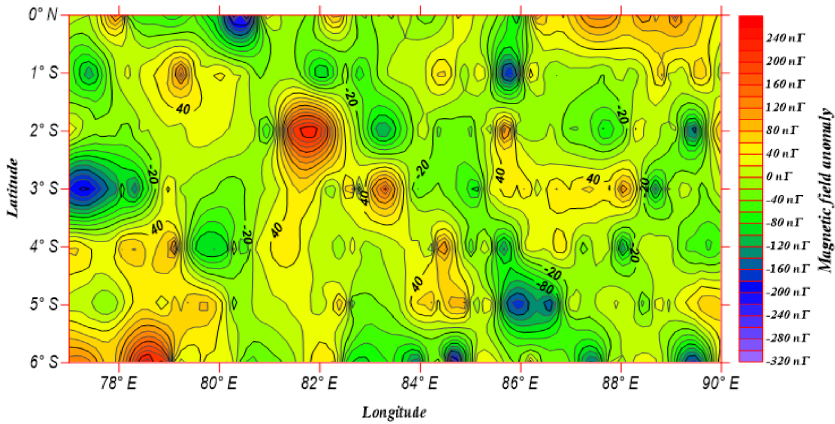


Fig. 2d. Magnetic anomaly map of the study area.

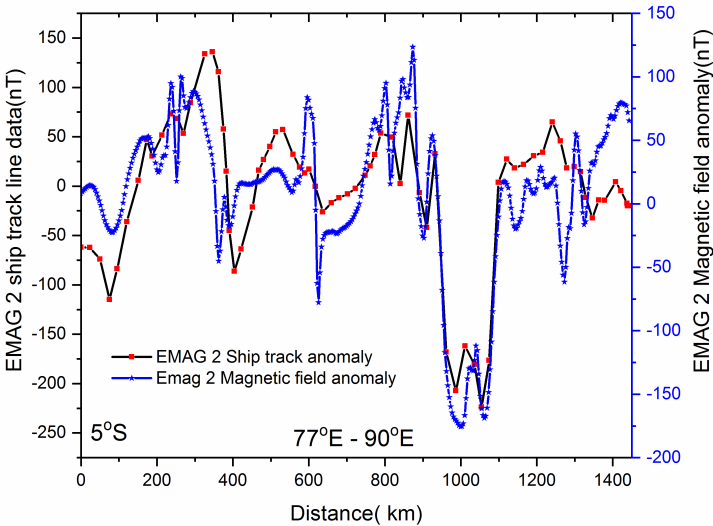


Fig. 2e. Comparison of EMAG 2 Magnetic field data with Ship track line data.

magnetic field anomaly data at an altitude of 4 km above mean sea level and is used for the calculation of Spectral and Werner depths.

3.2. Methodology

Determining anomalous geological subsurface structure is an important parameter in any of the geophysical methods. Spectral and Werner deconvolution techniques were widely used to determine the appropriate depth of the causative sources. *Subrahmanyam and Gebissa (2017)* carried out a performance analysis for these two techniques and showed the efficacy and limits of their usage for determining the tentative depths of the causative geological features.

The magnetic anomalies are interpreted with spectral and Werner deconvolution methods. Both methods provide depth to the interfaces. Each magnetic Profile was divided into several segments and segmentation was done with the knowledge of the magnetic lineation (age anomalies). Each segment overlaps with the adjacent segment by 5–10%. The magnetic anomalies were converted into the frequency domain and the amplitude spectrum was calculated. From this amplitude spectrum depths to the interfaces have been determined. The spectral method gives depths to the shallow, intermediate, and deepest layers from the selection of suitable filter. The slopes of the Fourier spectrum give depths on various layers.

Several frequencies (0.04 Hz, 0.06 Hz, 0.08 Hz, 0.1 Hz, and 0.12 Hz) were applied to extract the long-wavelength anomalies as shown in Fig. 2f. The Curie isotherm depth was measured for magnetic anomaly data using a spectral method with an appropriate filter (0.08 Hz, low pass). Curie-point depth is the depth at which rocks lose their ferromagnetic magnetization because of an increase in the temperature in the crust above the Curie temperature. So, the depth to the bottom of magnetic sources (DBMS) was used as an estimate of the Curie-point depth and therefore as a proxy for the temperature at depth (*Bansal et al., 2011*). When the random sources assumption is valid and clear spectral peaks with multiple points are present, and then it is possible to determine the depth to the bottom more reliably (*Ravat et al., 2007*).

The Free-air anomaly profiles are digitized in one kilometre interval and separated into various segments. Each segment is interpreted with the spec-

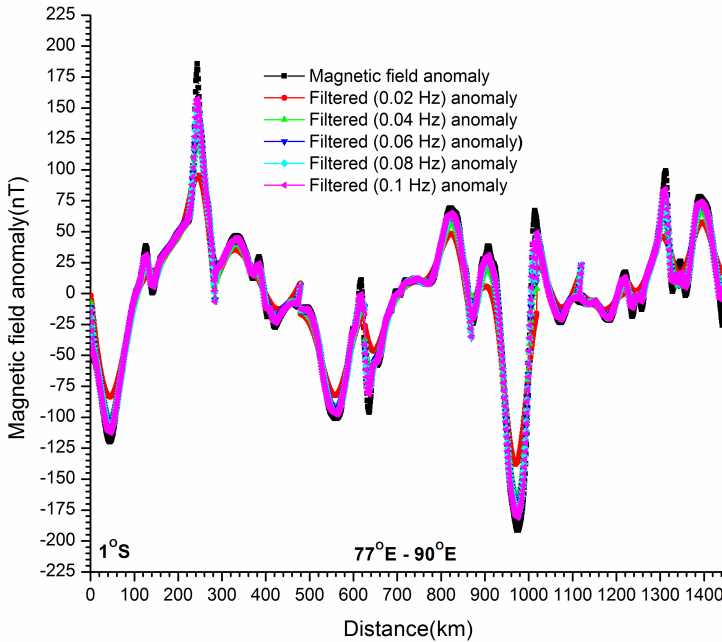


Fig. 2f. Filtered magnetic anomaly segments of Profile-1 (1°S, 77°E–90°E, length 1442 km).

tral method as explained above to find the basement and deeper depths of the oceanic crust. The depths obtained from spectral and Werner methods are correlated with 2D forward modelling results along with available densities obtained from velocity-density relation.

The Geosoft software has been used to improve the efficiency and speed of the calculations and to make them better suited to an interactive environment. The GM-SYS Profile inversion routine uses the Marquardt inversion algorithm (*Marquardt, 1963*) to linearize and invert the calculations. GM-SYS Profile inversion routine uses an implementation of that algorithm for gravity data which is developed by the USGS. GM-SYS Profile inversion uses a two-dimensional, flat-earth model for gravity calculations. 2D density models were calculated from input densities with known seismic velocities of oceanic crust from the velocity-density relationship (*Christensen and Wilkens, 1982*). The input depths for density modelling were taken from Spectral depths (unfiltered and filtered) of gravity data (*Ravi Kumar and Subrahmanyam, 2020*).

4. Results

Each gravity and magnetic profile was divided into different segments. Each segment was subjected to spectral and Werner deconvolution techniques for magnetic anomalies and spectral technique for Free-air anomaly. The profile-wise discussion was given below. All the gravity and magnetic profiles were taken in the W–E direction to identify crustal deformation between 77°E–90°E and the distance is about 1442 km.

4.1. Determination of the depths of bathymetry, sediments, and crust along profiles

The spectral deconvolution technique is used for gravity and magnetic data with various frequencies as input parameters to filter the shallow and deeper depths. Werner deconvolution technique was used to determine the shallow and deeper depths of unfiltered and filtered magnetic anomalies of each segment (*Ravi Kumar and Subrahmanyam, 2020*).

The Free-air anomaly data is useful in regional geophysical investigations as it contains information down to very short wavelengths (< 20 km). However, this is a tentative crustal structure, so the effect of the sediment is almost ignored. Each Free -air anomaly profile was divided into several segments and each segment overlaps with the adjacent segment by 5–10%. The Free-air anomalies were converted into the frequency domain and the amplitude spectrum was calculated. From this amplitude spectrum depth to the interface has been determined. For determining the deeper marker, the anomalies have been filtered with a low pass filter to extract the long-wavelength anomalies. The low pass filter of 0.08 Hz has been found suitable to represent the deeper interface of the oceanic crust. The same procedure is applied to magnetic data for the calculation of spectral and Werner depths.

The sediment thickness is almost negligible at the 85°E ridge and the average depth of the 85°E ridge is nearly 6. km (*Sreejith et al., 2011*) and the width of the ridge is nearly 65 km. The ridge is completely buried under the sediments (*Sreejith et al., 2011*) and has a density of 2.65 g/cm³ with sediments of a density of 2.3 g/cm³). So, the thickness of the sedimentary layer is less on the crest of the ridge and increases on either side, and the sediment load flattens the flanks of the deflection caused by the ridge load. The upper crust is thin and varies thickness up to 6 km except at the NER.

The crustal thickness is maximum (9 to 10 km) at the NER (*Radhakrishna et al., 2010*) and again decreases towards the eastern direction. The density of the upper crust is nearly 2.65 g/cm^3 and extremely thin at 85°E ridge. The lower crustal thickness varies up to 6 km and has a density of 2.95 g/cm^3 . The NER is elevated up to 2 km concerning the surrounding Bengal fan sediment's oceanic crust. The NER shows gravity high of about 21 mGal. The NER gravity field is interpreted as given isostatic compensation (*Mukhopadhyay and Krishna, 1995*) by utilizing available seismic constraints. The compensatory mass at the crustal base underlying the NER as interpreted from the gravity modelling suggests hot spot activity. The mantle has a density of 3.27 g/cm^3 and has hot spot activity which suggests a compensation mechanism (*Mukhopadhyay and Krishna, 1995*) of NER. The density of mantle plumes is 3.0 g/cm^3 and thickness varies from 6 to 8 km. So, deformations extend within the Indian Ocean plate which may produce large magnitude intraplate seismicity along the NER. The ANS is compensated by flexure of the crustal layer up to the extent of 1.5 km and has 8 km thick magmatic rocks in the lower crust (*Krishna, 2003*). Most of the sediments on the NER are categorized as pelagic, so we can understand that the rate of sediment build-up on the ridge has been slower than in other parts of the ocean.

4.1.1. Interpretation of the Profiles

Profile-1

Based on the anomaly pattern of the magnetic anomaly Profile-1 (1°S , 77°E – 90°E) was divided into nine segments.

Similarly, the gravity profile was divided into twelve segments based on anomaly patterns as shown in Table 1. For magnetic data, the depths to the top of the basement vary in the range of 3.4 to 5.3 km in respect of the spectral technique and 4–6 km for the Werner technique. The bottom depths from the spectral technique vary in the range of 8–13 km whereas Werner depth shows a 9–12 km range.

For gravity data, the depths to the basement vary in the range of 4 to 6 km but deeper depths show a variation of 8.5 to 11 km. The depths in Fig. 3a, shows undulations of oceanic crust, which is indicative of deformations. The thickness of the crust deciphered from gravity is thin when

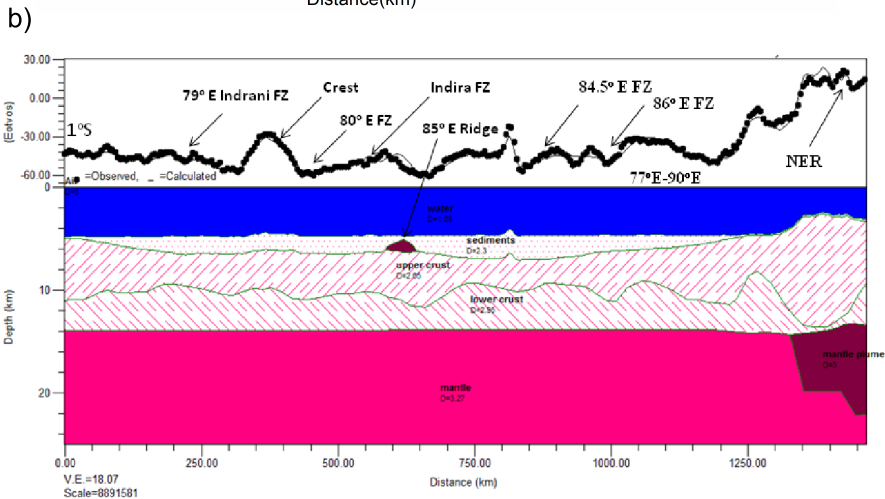
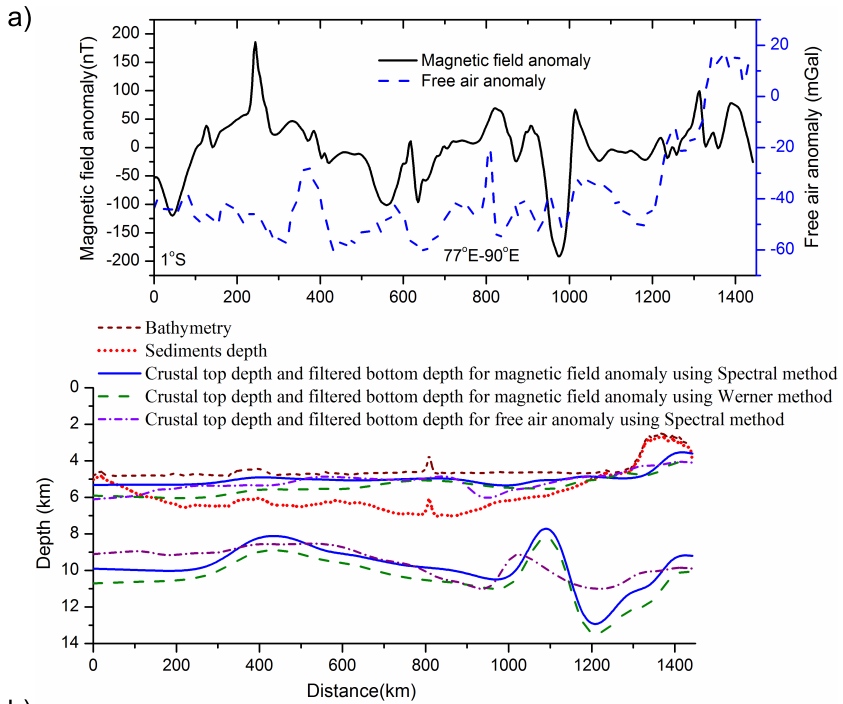


Fig. 3. Combined depth structure of magnetic and Free-air anomaly along Profile-1 (a); 2D Gravity model along Profile-1 (1°S, 77°E–90°E) (b).

compared to crustal thickness obtained from magnetic data.

This gravity anomaly profile-1 (1°S , 77°E – 90°E) as shown in Fig. 3b has bathymetry which is almost uniform (4.7 km) up to 1300 km towards the eastern direction. It decreases gradually and minimum (~ 2690 m) at the 90°E ridge. The sediment thickness gradually increases toward the eastern direction and becomes maximum at nearly 830 km but minimum at the NER. The sediment thickness is almost negligible at 85°E ridge.

Profile-2

The magnetic anomaly Profile-2 (2°S , 77°E – 90°E) was divided into seven segments. The depths to the top of the basement vary in the range of 4 to 6 km for the spectral technique and 4.2–5.2 km in the case of the Werner technique. The bottom depths from spectral technique and Werner techniques change in the range of 9–11.2 km and 10–12 km range respectively (Table 1). The depths obtained from both magnetic and gravity (only spectral) has been used to draw a tentative structure of the oceanic crust (Fig. 4a) and these depths show undulations of oceanic crust towards the eastern side of the profile. It was observed that the thickness of the crust deciphered from gravity was thin when compared to magnetic data. However, there is a good agreement between the spectral and Werner depths of magnetic data. The gravity profile was subdivided into five segments, as shown in Table 1 where depths to the basement vary in the range of 4.5–6 km, and deeper depths have a variation of 9 to 11.5 km.

The gravity anomaly profile-2 (2°S , 77°E – 90°E) has bathymetry shown in Fig. 4b is gradually decreasing towards the eastern direction and minimum (~ 2800 m) at 90°E ridge. The sediment thickness gradually increases toward the eastern direction and becomes minimum at 85°E ridge, but on both sides of the ridge, sediment thickness increases. The average depth of the 85°E ridge is nearly 6 km and the width of the ridge is nearly 110 km. The thickness of the sedimentary layer is less on the crest of the 85°E ridge but increases on either side. A gravity high of 28 mGal is observed due to tectonic features like seamounts. The upper crust is thin with undulations and crustal thickness is up to 9 km at the NER. The lower crust has a thickness that varies up to 9 km and its density is nearly 2.95 g/cm^3 . The NER is elevated up to 2 km concerning surrounding Bengal fan sediments oceanic crust which shows gravity high of about 15 mGal.

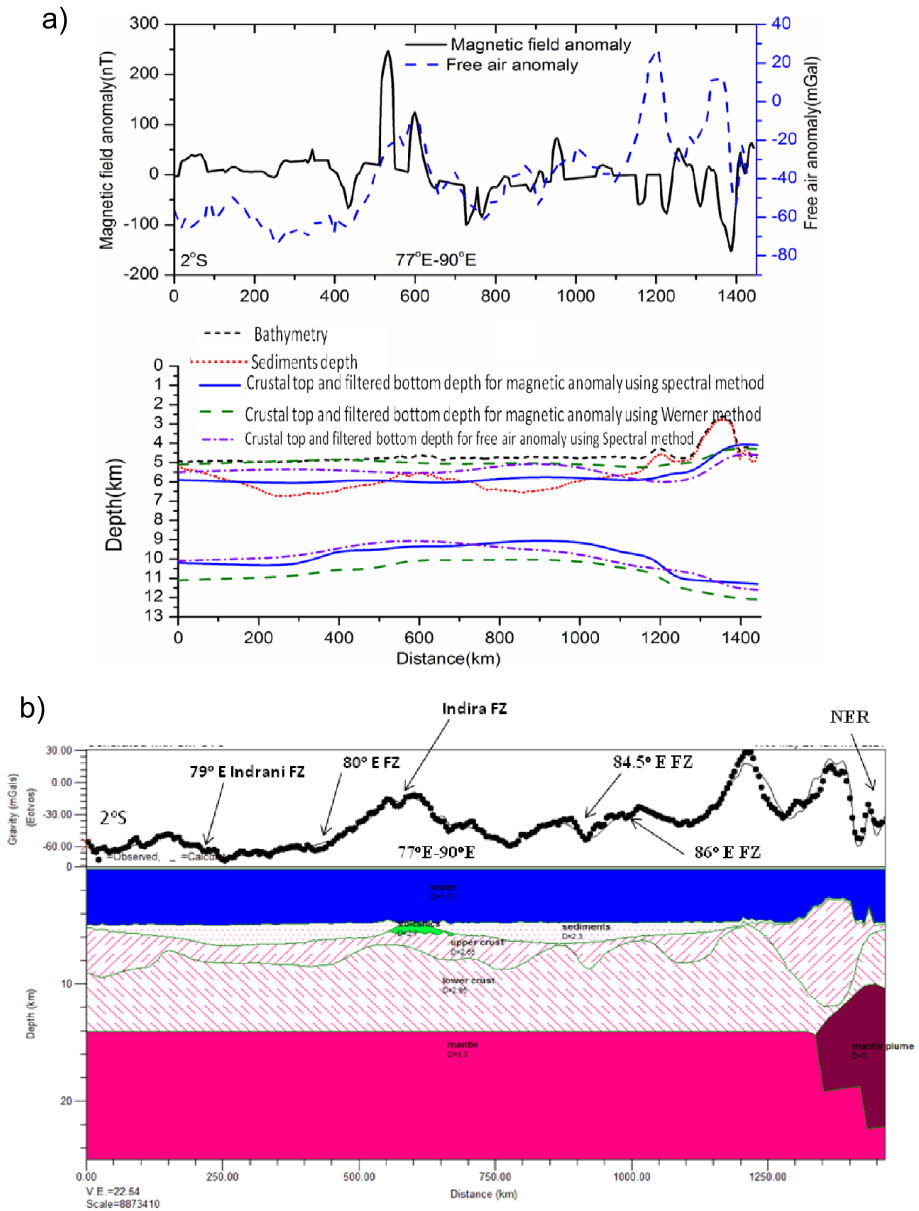


Fig. 4. Combined depth structure of magnetic and Free-air anomaly along Profile-2 (a); 2D Gravity model along Profile-2 (2°S, 77°E–90°E) (b).

Table 1. Spectral and Werner depths along profiles.

Magnetic profile-1							Free-air anomaly profile-1			
			Spectral depths (km)		Werner depths (km)				Spectral depths (km)	
Segment	Segment length (km)	Bathymetry (km)	Unfiltered (Z ₁)	Filtered (Z ₂)	Unfiltered (Z ₁)	Filtered (Z ₂)	Segment	Segment length (km)	Unfiltered (Z ₁)	Filtered (Z ₂)
SM1-1	0–284	4.8	5.3	10	5	9	SG1-1	0–120	6	9
SM1-2	280–479	4.5	4.8	8	6	10	SG1-2	115–186	5.5	9.1
SM1-3	450–625	4.6	5	9	5.5	10	SG1-3	179–306	5.3	9.0
SM1-4	626–869	4	4.3	9.8	5	11	SG1-4	305–448	5.3	8.5
SM1-5	868–1018	4.6	5.3	10.5	6	10	SG1-5	441–600	4.8	8.5
SM1-6	1010–1120	4.6	5.0	8.5	5	10	SG1-6	601–774	5	9.5
SM1-7	1120–1228	4.5	4.8	13	5	12	SG1-7	771–883	4.8	10.5
SM1-8	1227–1343	2.8	3.5	11	3.8	10	SG1-8	878–962	6	11
SM1-9	1344–1442	2.6	3.4	9.1	4	10.5	SG1-9	963–1045	5.5	9
							SG1-10	1038–1260	4.8	11
							SG1-11	1261–1360	4.2	10
							SG1-12	1361–1442	4	9.8
Magnetic profile-2							Free-air anomaly profile-2			
SM2-1	0–304	4.6	6	10.3	5	11	SG2-1	0–305	5.4	10
SM2-2	290–477	4.4	5.96	9.5	4.8	10.5	SG2-2	298–679	5.5	9
SM2-3	469–684	4.6	6	9.3	5	10	SG2-3	675–990	5.0	9.5
SM2-4	672–1023	4.0	5.7	9	5	10	SG2-4	975–1290	6	10.5
SM2-5	1001–1181	4.6	5.93	9.7	5.2	10.5	SG2-5	1286–1442	4.5	11.5
SM2-6	1177–1284	4.5	5.5	11	5	11.5				
SM2-7	1274–1442	3.5	4	11.2	4.2	12				
Magnetic profile-3							Free-air anomaly profile-3			
SM3-1	0–270	4.7	5.5	10.2	5	11	SG3-1	0–360	5.0	10
SM3-2	240–570	4.8	6.0	10	5.5	10.6	SG3-2	358–824	4.5	10.4
SM3-3	567–675	3.0	4.0	10.7	3.5	10.5	SG3-3	803–1169	4.5	10.3
SM3-4	670–857	2.8	3.5	10.4	4	10	SG3-4	1162–1442	3.6	7.5
SM3-5	853–1186	4.6	5.5	10.7	5	11.5				
SM3-6	1144–1442	3.2	4.0	8.2	3.8	9				
Magnetic profile-4							Free-air anomaly profile-4			
SM4-1	0–139	4.8	5.0	8.2	5.2	8.5	SG4-1	0–460	5	8
SM4-2	138–228	4.9	5.2	8.5	5.3	9	SG4-2	458–780	4.5	9
SM4-3	225–779	3.5	4	8.3	4.3	9	SG4-3	767–1120	6	10
SM4-4	775–1140	4.7	5.2	9.5	5	10	SG4-4	1118–1442	4	11
SM4-5	1135–1442	2.6	3.5	11.6	3.2	12.4				

Table 1. Continued from the previous page.

Magnetic profile-5							Free-air anomaly profile-5			
SM5-1	0–157	4.8	6	9.3	5.2	10	SG5-1	0–298	5.5	8.8
SM5-2	150–439	5.0	5.96	10.6	5.5	11	SG5-2	292–528	5.2	9.5
SM5-3	430–654	3.7	6	9	5.5	8.5	SG5-3	525–832	6.5	10
SM5-4	650–926	4.2	5.96	9.8	6	10	SG5-4	817–1234	5.5	11.3
SM5-5	921–1140	4.8	6	11	5.3	11.2	SG5-5	1230–1442	4.6	10.4
SM5-6	1138–1288	4.5	6	11	5.2	11.5				
SM5-7	1183–1442	3.4	4.4	10.8	5	11				
Magnetic profile-6							Free-air anomaly profile-6			
SM6-1	0–460	5.0	6.6	10	6	11	SG6-1	0–170	5.2	10.5
SM6-2	461–724	5.1	6.1	10.3	5	12	SG6-2	165–311	5.5	10.8
SM6-3	725–950	5.2	8	13.5	6	13	SG6-3	303–410	6.5	11.2
SM6-4	951–1055	4.8	5.2	10.38	5	9	SG6-4	406–600	5.3	9.5
SM6-5	1056–1275	4.5	8	11.9	6	13	SG6-5	598–926	5.6	9.8
SM6-6	1276–1442	3.8	5	8.3	4	10	SG6-6	920–1442	5.1	9

Profile 3

The magnetic anomaly Profile-3 (3°S, 77°E–90°E) was divided into six segments based on anomaly pattern and depths to the top and bottom of the basement (Table 1). The spectral analysis yields depths to the shallow and deeper layers in the range of 3.5–6 km and 8.2–10.7 km respectively. The depths determined from Werner deconvolution are in the range of 3.5–5.5 km and 9–11.5 km respectively to shallow and deeper layers.

The gravity profile is divided into four segments (Table 1) and the depths to the basement vary in the range of 3.6–5 km and deeper depths show the variation of 7.5–10.4 km. The depths to the top and bottom of each anomaly segment have shown variations and are used to draw a tentative structure of the oceanic crust (Fig. 5a). These depths show undulations and the thickness of the crust deciphered from gravity is thin and shallow when compared to magnetic data.

This gravity anomaly profile-3 (Fig. 5b) has bathymetry which is gradually decreasing towards the eastern direction and becomes minimum (~2000 m) at the ANS. The sediment thickness is almost uniform and becomes minimum at the ANS. The average bottom depth of the ANS is nearly 10 km and the width is almost 150 km.

The ANS is completely buried under the sediments with sediments of a

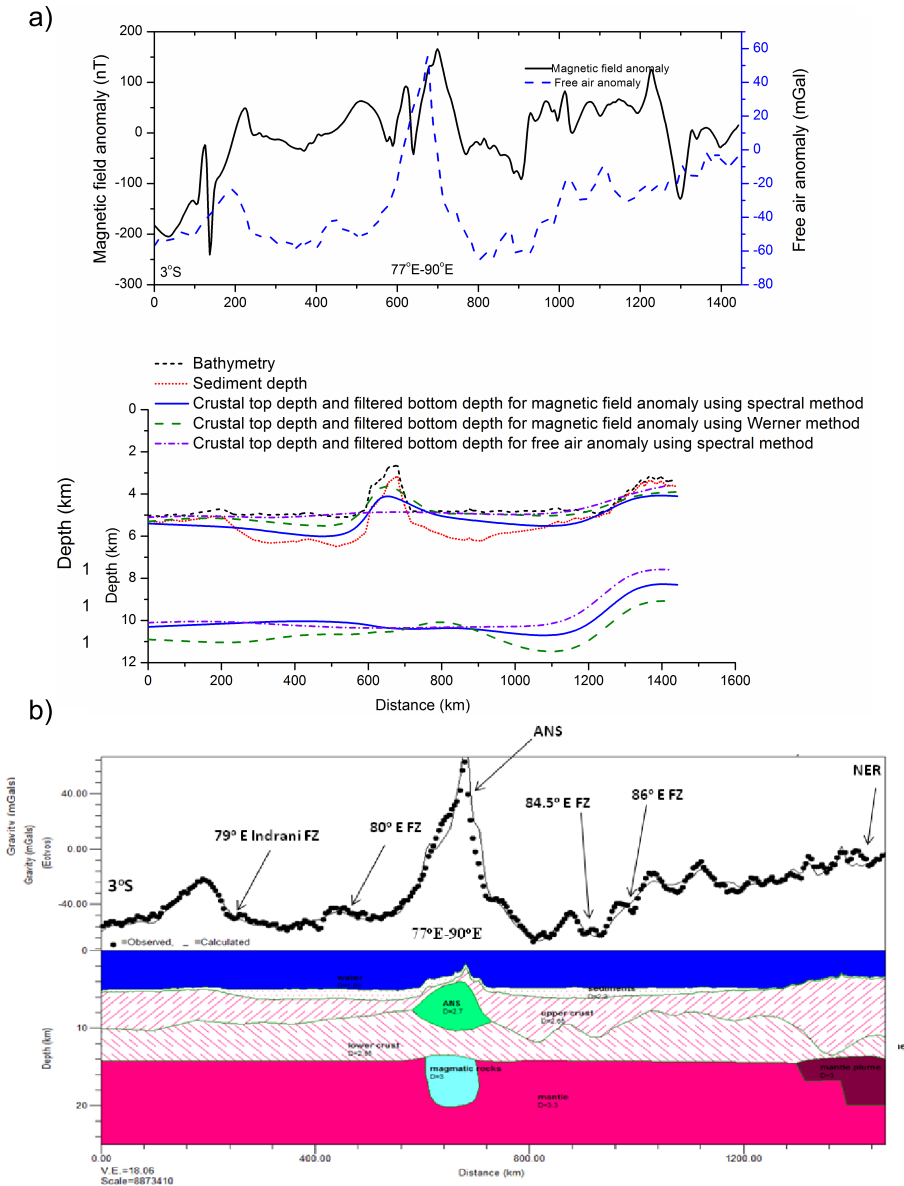


Fig. 5. Combined depth structure of magnetic and Free-air anomaly along Profile-3 (a); 2D Gravity model along Profile-3 (3°S, 77°E–90°E) (b).

density of 2.3 g/cm^3 . The thickness of the sedimentary layer is less on the crest of the ANS and increases on either side. Underneath buried hills and 85°E Ridge, the crust is down flexed up to 2.5 km in response to volcanic loads. The upper crust is thin and has undulations except at the NER.

The crustal thickness is maximum (up to 10 km) at the NER (*Radhakrishna et al., 2010*) and the density of the upper crust is nearly 2.65 g/cm^3 and extremely thin (0.5 km) at the ANS. The lower crustal thickness varies up to 6 km and has a density of 2.95 g/cm^3 .

Profile 4

The magnetic anomaly profile (4°S , 77°E – 90°E) was divided into five segments. The depths to the top and bottom of the basement have been determined and shown in Table 1. The depths to the top of the magnetic basement vary in the range of 3.5–5.2 km and bottom depths (Curie isotherm) vary in the range of 8.2–11.6 km. The unfiltered and filtered magnetic anomalies of each segment were then subjected to the Werner deconvolution technique and depths to the top of the basement vary in the range of 3.2–5.2 km whereas bottom depths show a variation of 8.5–12.4 km (Table 1). These two (Spectral and Werner) depths sections are in good agreement.

The gravity profile is divided into four segments (Table 1) and depths to the basement vary in the range of 4–6 km while deeper depths show a variation of 8–11 km. The depths obtained from both magnetic and gravity (only spectral) have been used to draw a tentative structure of the oceanic crust (Fig. 6a) and these depths show undulations of oceanic crust indicative of deformations.

The bathymetry corresponding to the gravity anomaly profile (Fig. 6b) is nearly 5000 m and becomes minimum (2700 m) at the NER. The sediment thickness is minimum at the NER and ANS. The average bottom depth of the ANS is nearly 8 km and the width of the seamount is nearly 110 km. The ANS is completely buried under the sediments and has a density of 2.7 g/cm^3 . The sediments have a density of 2.3 g/cm^3 . The thickness of the sedimentary layer is less on the crest of the ANS and increases on either side.

Profile 5

The magnetic anomaly of the Profile-5 (5°S , 77°E – 90°E) was divided into

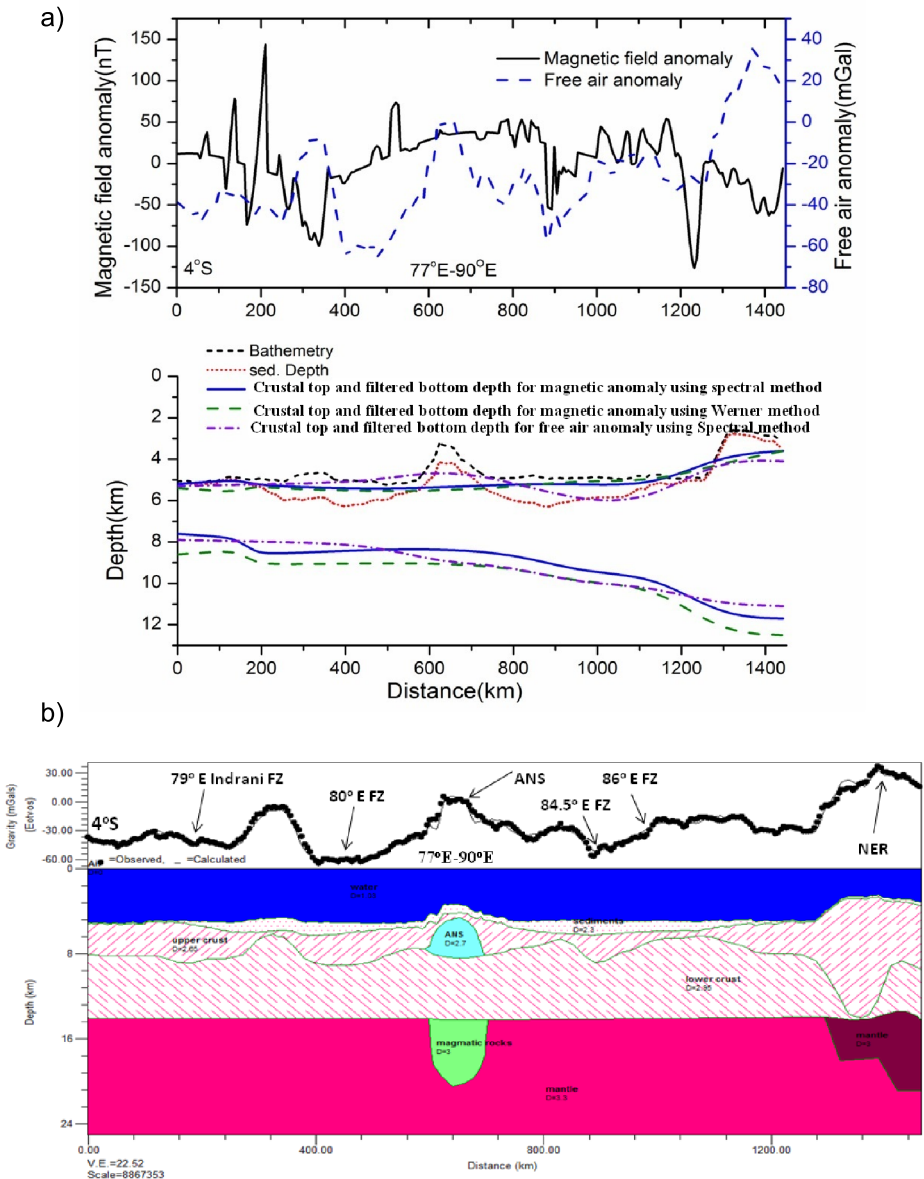


Fig. 6. Combined depth structure of magnetic and Free-air anomaly along Profile-4 (a); 2D Gravity model along Profile-4 (4°S, 77°E–90°E) (b).

seven segments. The depths to the top and bottom of the basement have been determined and these values are shown in Table 1. The unfiltered and filtered magnetic anomalies of each segment were then subjected to the Werner deconvolution technique. The depths to the top of the basement vary in the range of 4.4–6 km in respect of the spectral technique and 5–6 km for the Werner technique. The bottom depths from the spectral technique vary in the range of 9–11 km, whereas Werner depth shows an 8.5–11.5 km range (Table 1). The spectral and Werner depths to the top and bottom of oceanic crust are in good agreement.

In the same way gravity profile was divided into five segments (Table 1) and the depths to the basement vary in the range of 4.6–6.5 km while deeper depths revealed the variation of 8.8–11.3 km. The depths to the top and bottom of each anomaly segment obtained from these two techniques have shown variations and are used to draw a tentative structure of the oceanic crust (Fig. 7a). These depths show undulations of oceanic crust indicative of deformations and the thickness of the crust deciphered from gravity was thin and shallow when compared to magnetic data.

The gravity anomaly profile-5 (5°N, 77°E–90°E) corresponding bathymetry (Fig. 7b) is almost uniform (up to 5000 m) towards the eastern direction and becomes minimum (3500 m) at the NER. The sediment thickness is minimum corresponding to the ANS and NER. The average bottom depth of the ANS is nearly 7.7 km and the seamount is buried under the sediments and has a density of 2.7 g/cm³ with sediments of the density of 2.3 g/cm³. The ANS is compensated by flexure of the crustal layer up to the extent of ~1.5 km and having 8 km thick magmatic rocks in the lower crust.

The thickness of the sedimentary layer is less on the crest of the ANS and increases on either side. The upper crust is extremely thin and undulating but thickness increases at the NER. The lower crustal thickness varies up to 10 km and has a density of 2.95 g/cm³. The density of mantle plumes is 3.0 g/cm³ and thickness varies from 3 to 6 km. So, deformations extend within the Indian Ocean plate which may produce large magnitude intraplate seismicity along the NER. The average sediment thickness is negligible above 90°E ridge and is composed of sub-alkaline basalt rocks.

Profile 6

The magnetic anomaly of this profile (6°S, 77°E–90°E) was divided into six

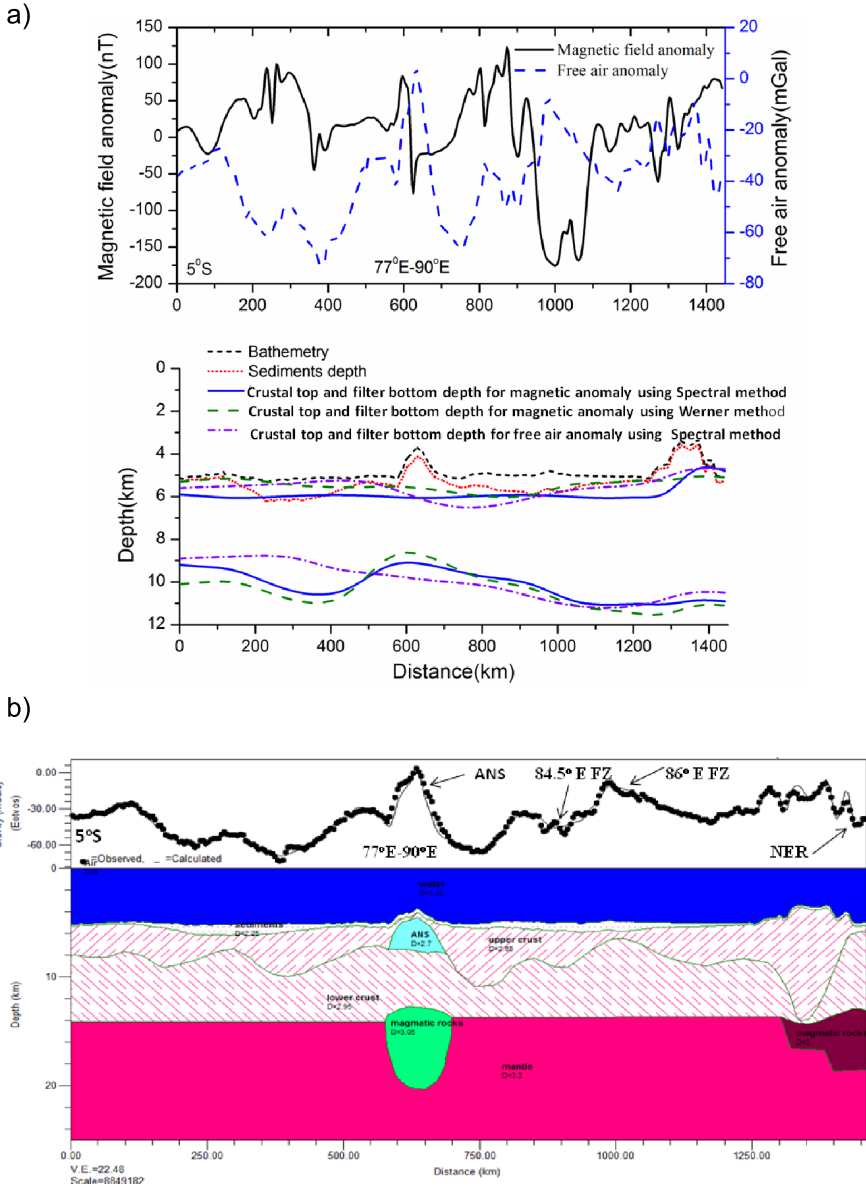


Fig. 7. Combined depth structure of magnetic and Free-air anomaly along Profile-5 (a); 2D Gravity model along Profile-5 (5°S, 77°E–90°E) (b).

segments. The spectral and Werner depths for this profile were determined and the same procedure is carried out for all six segments. The depths to the top of the basement vary in the range of 5–8 km in respect of the spectral technique and 4–6 km for the Werner technique. The bottom depths from the spectral technique vary in the range of 8.3–13.5 km, whereas Werner depth shows a 9–13 km range (Table 1). The gravity profile was divided into six segments (Table 1) and the depths to the basement vary in the range of 5.1–6.5 km while deeper depths show a variation of 9–11.2 km. The depths to the top and bottom of each anomaly segment obtained from these two techniques have shown variations and are used to draw a tentative structure of the oceanic crust (Fig. 8a). These depths shows undulations of oceanic crust and the thickness of the crust deciphered from gravity is thin and shallow when compared to magnetic data.

The gravity model of the Profile-6 (6°S, 77°E–90°E) is shown in Fig. 8b having bathymetry is almost uniform (5200 km) towards an eastern direction and becomes minimum at the NER. The sediment thickness is the minimum corresponding to the NER. The thickness of the sedimentary layer is maximum up to 1 km at a distance of 270 km from the origin and decreases gradually towards the eastern direction. The upper crust is almost thin, but the lower crustal thickness varies up to 6 km and has a density of 2.95 gm/cm³. The Crustal thicknesses as obtained by various methods are shown in Figs. 9a, b, c.

5. Conclusions

The gravity and magnetic data south of Sri Lanka, covering the area between 1°S to 6°S and 77°E–90°E, have been subjected to interpretation by spectral and Werner deconvolution techniques. Both methods were applied to magnetic field data and slopes of the Fourier spectrum give depths to shallow and deeper layers. Similarly, the spectral method was applied to gravity data to obtain depths of shallow and deeper layers. The plot of these depths along with the profiles 1–6 in the W–E direction shows the tentative crustal structure of the study area. On analysing these crustal structures and the interpreted 2D gravity modelling results, one can easily decipher those depths to the basement and its bottom is undulating along with the profiles. Our results confirm deformation in the oceanic crust, which

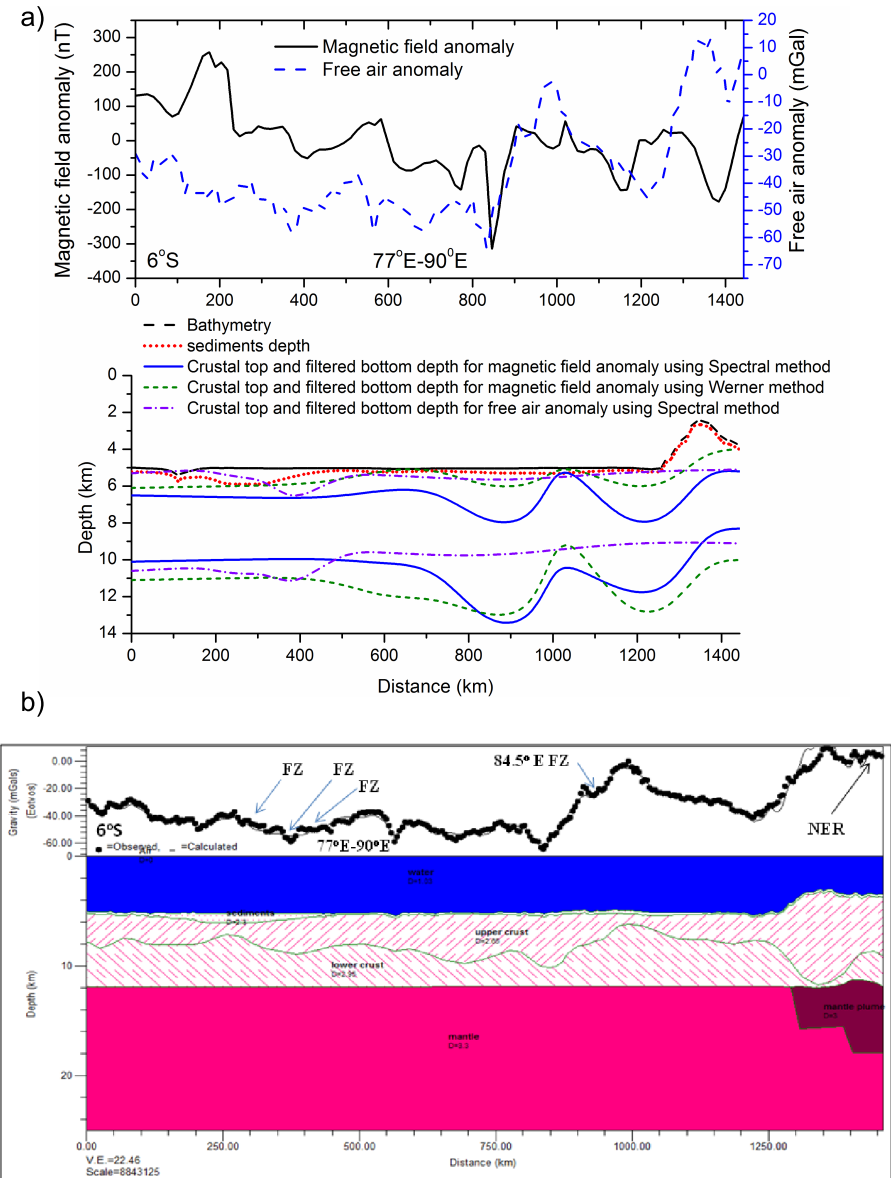


Fig. 8. Combined depth structure of magnetic and Free-air anomaly along Profile-6 (a); 2D Gravity model along Profile-6 (6°S, 77°E–90°E) (b).

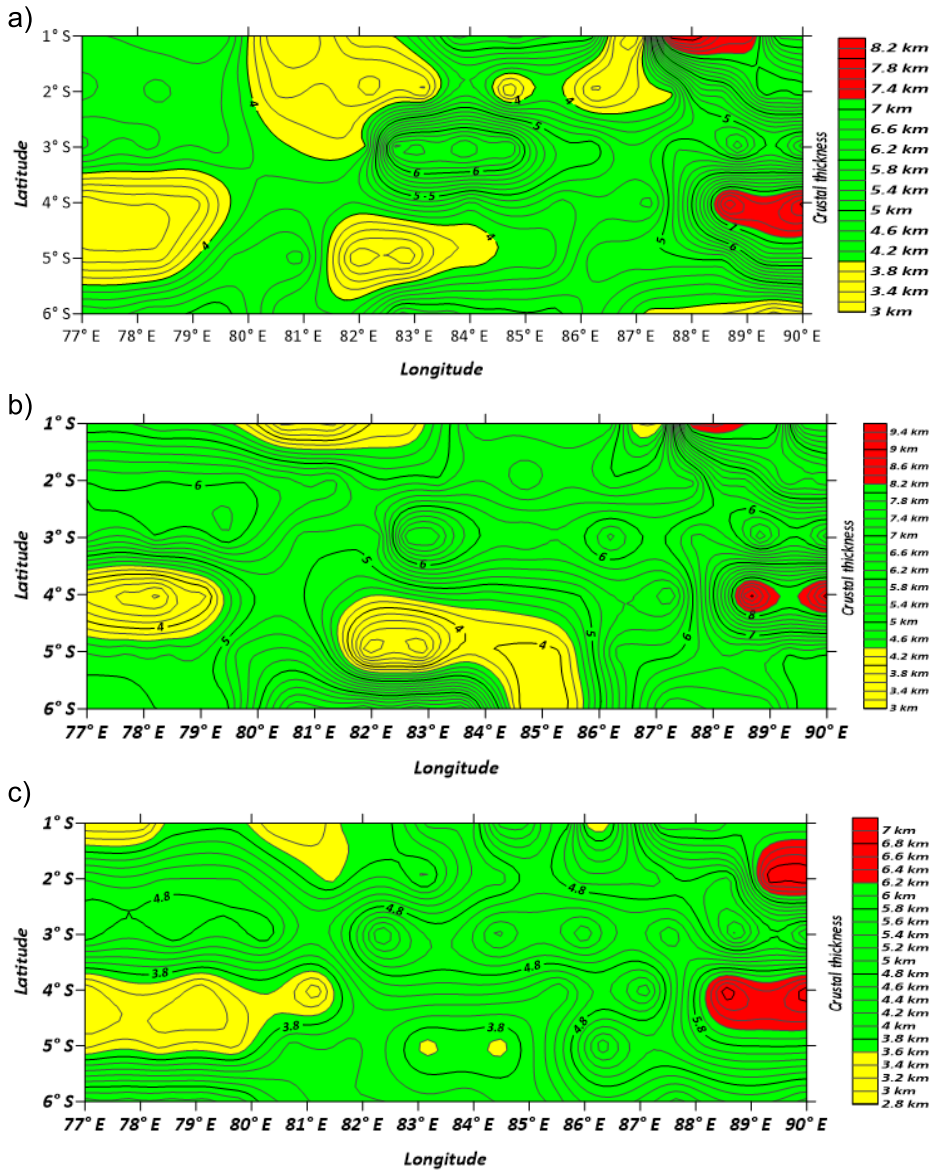


Fig. 9. Crustal thickness contour map for the magnetic data from the spectral method (a); for the magnetic data from the Werner method (b); and for the Free-air gravity data from the spectral method (c).

was established on the basis of previous seismic reflection studies.

No quantitative interpretation and modelling of gravity data has yet been done systematically. In this study, we have considered a large area and first attempted to determine the depths of the shallow and deeper interfaces of the oceanic crust based on the spectral and Werner deconvolution techniques. The crustal top depths vary in the range of 3.5–8 km and the bottom depth varies in the range of 8.2–13.5 km for magnetic field anomaly data using the spectral method. The crustal top depth varies in the range of 3.2–6 km and bottom depths in the range of 8.5–13 km from magnetic field anomaly applying the Werner method. The spectral method for Free-air anomaly data indicates that the crustal top depths change in the range of 3.6–6.5 km, while the bottom depth is in the range of 7.5–11.5 km. The significant finding is that the crustal top depths obtained from spectral and Werner techniques of magnetic data were nearly the same, which reduces ambiguity. The average depth to the top of the oceanic crust varies in the range of 4 to 6 km, whereas bottom depths are 7 to 11 km. The thickness of the oceanic crust (Figs. 9a, c) is up to a maximum of 9.6 km and the crustal thickness is increasing towards the eastern side, while it decreases towards the northern side.

All the tentative crustal structures show an undulating pattern, indicative of folding and faulting patterns. From the crustal depth structures, obtained from Free-air and magnetic anomaly profiles, one can see the undulating nature of the basement which corresponds to shallow and deeper sources. The deeper sources represent the low-frequency component by the steep gradient of the amplitude spectrum. On the other hand, shallow magnetic bodies represent high-frequency components having fewer steep gradients. The deeper magnetic sources were attributable to magnetic bodies of the basement surface and the shallow sources were probably regarded as magnetic intrusions.

Acknowledgements. The authors express their sincere thanks to anonymous reviewers and expect valuable suggestions in improving the quality of the paper.

Compliance with ethical standards. The authors declare that they have no conflict of interest and adhere to copyright norms.

References

- Bansal A. R., Gabriel G., Dimri V. P., Krawczyk C. M., 2011: Estimation of the depth to the bottom of magnetic sources by a modified Centroid method for fractal distribution of sources: an application to aeromagnetic data in Germany. *Geophysics*, **76**, 3, L11–L22, doi: 10.1190/1.3560017.
- Bercovici D., Wessel P., 1994: A continuous kinematic model of plate-tectonic motions. *Geophys. J. Int.*, **119**, 2, 595–610, doi: 10.1111/j.1365-246X.1994.tb00144.x.
- Bird P., 2003: An updated digital model of plate boundaries. *Geochem. Geophys. Geosyst.*, **4**, 3, doi: 10.1029/2001GC000252.
- Bull J. M., Scrutton R. A., 1990: Fault reactivation in the central Indian Ocean and the rheology of oceanic lithosphere. *Nature*, **344**, 6269, 855–858, doi: 10.1038/344855a0.
- Bull J. M., Martinod J., Davy P., 1992: Buckling of the oceanic lithosphere from geophysical data and experiments. *Tectonics*, **11**, 3, 537–548, doi: 10.1029/91TC02908.
- Christensen N. I., Wilkens R. H., 1982: Seismic properties, density, and composition of the Icelandic crust near Reydarfjörður. *J. Geophys. Res. Solid Earth*, **87**, B8, 6389–6395, doi: 10.1029/JB087iB08p06389.
- Curray J. R., Emmel F. J., Moore D. G., Raitt R. W., 1982: Structure, tectonics, and geological history of the northeastern Indian Ocean. In: Nairn A. E. M., Stehli F. G. (Eds.): *The Ocean Basins and Margins*. Springer, Boston, MA, 399–450, doi: 10.1007/978-1-4615-8038-6_9.
- Curray J. R., Munasinghe T., 1991: Origin of the Rajmahal Traps and the 85°E Ridge: Preliminary reconstructions of the trace of the Crozet hotspot. *Geology*, **19**, 12, 1237–1240, doi: 10.1130/0091-7613(1991)019<1237:00TRTA>2.3.CO;2.
- Curray J. R., 1994: Sediment volume and mass beneath the Bay of Bengal. *Earth Planet. Sci. Lett.*, **125**, 1-4, 371–383, doi: 10.1016/0012-821X(94)90227-5.
- Das P., Iyer S. D., Kodagali V. N., Krishna K. S., 2005: Distribution and origin of seamounts in the Central Indian Ocean Basin. *Mar. Geod.*, **28**, 3, 259–269, doi: 10.1080/01490410500204637.
- Das P., Iyer S. D., Kodagali V. N., 2007: Morphological characteristics and emplacement mechanism of the seamounts in the Central Indian Ocean Basin. *Tectonophysics*, **443**, 1-2, 1–18, doi: 10.1016/j.tecto.2007.08.002.
- DeMets C., Gordon R. G., Argus D. F., 1988: Intraplate deformation and closure of the Australia-Antarctica-Africa plate circuit. *J. Geophys. Res.*, **93**, B10, 11877–11897, doi: 10.1029/JB093iB10p11877.
- Desa M. A., Ramana M. V., 2021: Integrated analysis of magnetic, gravity and multichannel seismic reflection data along a transect southeast of Sri Lanka, Bay of Bengal: New constraints. *Mar. Geol.*, **438**, 106543, doi: 10.1016/j.margeo.2021.106543.
- Divya Bharathi R., Subrahmanyam M., Ramesh D. S., Rajendran S., 2020: Tentative model of crustal structure of the Central Indian Ocean deformation as inferred from spectral and Werner deconvolution techniques of magnetic data. *Curr. Sci.*, **119**, 9, 1526–1539, doi: 10.18520/cs/v119/i9/1526-1539.

- Duncan R. A., 1981: Hotspots in the southern oceans—an absolute frame of reference for motion of the Gondwana continents. *Tectonophysics*, **74**, 1-2, 29–42, doi: 10.1016/0040-1951(81)90126-8.
- GEBCO Compilation Group, 2019: The GEBCO_2019 Grid: a continuous terrain model of the global oceans and land. doi: 10.5285/836f016a-33be-6ddc-e053-6c86abc0788e.
- Geller C. A., Weissel J. K., Anderson R. N., 1983: Heat transfer and intraplate deformation in the central Indian Ocean. *J. Geophys. Res. Solid Earth*, **88**, B2, 1018–1032, doi: 10.1029/JB088iB02p01018.
- Goetze C., Evans B., 1979: Stress and temperature in the bending lithosphere as constrained by experimental rock mechanics. *Geophys. J. Int.*, **59**, 3, 463–478, doi: 10.1111/j.1365-246X.1979.tb02567.x.
- Gopala Rao D., Krishna K. S., Sar D., 1997: Crustal evolution and sedimentation history of the Bay of Bengal since the Cretaceous. *J. Geophys. Res. Solid Earth*, **102**, B8, 17747–17768, doi: 10.1029/96JB01339.
- Gopala Rao D., Krishna K. S., Neprochnov Yu. P., Grinko B. N., 2004: Satellite gravity anomalies and crustal features of the Central Indian Ocean Basin. *Curr. Sci.*, **86**, 7, 948–957, <https://www.jstor.org/stable/24109277>.
- Gordon R. G., DeMets C., Argus D. F., 1990: Kinematic constraints on distributed lithospheric deformation in the equatorial Indian Ocean from present motion between the Australian and Indian plates. *Tectonics*, **9**, 3, 409–422, doi: 10.1029/TC009i003p00409.
- Goslin J., Philippe P., 1984: Absolute and relative plate motions and hypotheses on the origin of five aseismic ridges in the Indian Ocean. *Tectonophysics*, **101**, 3-4, 221–244, doi: 10.1016/0040-1951(84)90115-X.
- Haxby W. F., 1987: Gravity field of the world's oceans. Nat. Geophys. Data Ctr., NOAA, Boulder, CO.
- Hayes G. P., Moore G. L., Portner D. E., Hearne M., Flamme H., Furtney M., Smoczyk G. M., 2018: Slab2, a comprehensive subduction zone geometry model. *Science*, **362**, 6410, 58–61, doi: 10.1126/science.aat4723.
- Kalra R., Srinivasa Rao G., Fainstein R., Radhakrishna M., Bastia R., Chandrasekhar S., 2014: Crustal architecture and tectono-magmatic history of the western offshore of India: Implications on deepwater sub-basalt hydrocarbon exploration. *J. Pet. Sci. Eng.*, **122**, 149–158, doi: 10.1016/j.petrol.2014.07.002.
- Kamesh Raju K., 1993: Magnetic lineations, fracture zones and seamounts in the Central Indian Basin. *Mar. Geol.*, **109**, 3-4, 195–201, doi: 10.1016/0025-3227(93)90060-9.
- Krishna K. S., 1996: Tectonic model for the evolution of oceanic crust in the northeastern Indian Ocean from the late Cretaceous to the early Tertiary. *Oceanogr. Lit. Rev.*, **43**, 8, 803.
- Krishna K. S., Ramana M. V., Gopala Rao D., Murthy K. S. R., Malleswara Rao M., Subrahmanyam V., Sarma K. V. L. N. S., 1998: Periodic deformation of oceanic crust in the central Indian Ocean. *J. Geophys. Res. Solid Earth*, **103**, B8, 17859–17875, doi: 10.1029/98JB00078.

- Krishna K. S., Bull J. M., Scrutton R. A., 2001: Evidence for multiphase folding of the central Indian Ocean lithosphere. *Geology*, **29**, 8, 715–718, doi: 10.1130/0091-7613(2001)029<0715:EFMFOT>2.0.CO;2.
- Krishna K. S., Gopala Rao D., Neprochnov Yu. P., 2002: Formation of diapiric structure in the deformation zone, central Indian Ocean: A model from gravity and seismic reflection data. *J. Earth. Syst. Sci.*, **111**, 1, 17–28, doi: 10.1007/BF02702219.
- Krishna K. S., 2003: Structure and evolution of the Afanasy Nikitin seamount buried hills and 85°E Ridge in the northeastern Indian Ocean. *Earth Planet. Sci. Lett.*, **209**, 3-4, 379–394, doi: 10.1016/S0012-821X(03)00081-5.
- Krishna K. S., Bull J. M., Ishizuka O., Scrutton R. A., Jaishankar S., Banakar V. K., 2014: Growth of the Afanasy Nikitin seamount and its relationship with the 85°E Ridge, northeastern Indian Ocean. *J. Earth Syst. Sci.*, **123**, 1, 33–47, doi: 10.1007/s12040-013-0392-x.
- Liu C. S., Sandwell D. T., Curray J. R., 1983: The negative gravity field over the 85°E Ridge. *J. Geophys. Res. Solid Earth*, **87**, B9, 7673–7686, doi: 10.1029/JB087iB09p07673.
- Marquardt D. W., 1963: An algorithm for least-squares estimation of nonlinear parameters. *J. Soc. Indust. Appl. Math.*, **11**, 2, 431–441, doi: 10.1137/0111030.
- Maus S., Barckhausen U., Berkenbosch H., Bournas N., Brozena J., Childers V., Dostaler F., Fairhead J. D., Finn C., von Frese R. R. B., Gaina C., Golynsky S., Kucks R., Lühr H., Milligan P., Mogren S., Müller R. D., Olesen O., Pilkington M., Saltus R., Schreckenberger B., Thébaud E., Caratori Tontini F., 2009: EMAG2: A 2-arcmin resolution Earth Magnetic Anomaly Grid compiled from satellite, airborne, and marine magnetic measurements. *Geochem. Geophys. Geosyst.*, **10**, 8, 1–12, doi: 10.1029/2009GC002471.
- Morgan W. J., 1983: Hotspot tracks and the early rifting of the Atlantic. In: Morgan P., Baker B. H. (Eds.): *Processes of Continental Rifting*. *Tectonophysics*, **94**, 1-4, 123–139, Elsevier, doi: 10.1016/0040-1951(83)90013-6.
- Mukhopadhyay M., Krishna M. B. R., 1995: Gravity anomalies and deep structure of the Ninetyeast Ridge north of the equator, eastern Indian Ocean — a hot spot trace model. *Mar. Geophys. Res.*, **17**, 2, 201–216, doi: 10.1007/BF01203426.
- Mukhopadhyay R., Ghosh A. K., Iyer S. D., 2008: *Tectonics and Geomorphology*. *Handb. Explor. Environ. Geochem.*, **10**, 37–66, doi: 10.1016/S1874-2734(07)10002-4.
- Mukhopadhyay R., Ghosh A. K., Iyer S. D., 2017: *The Indian Ocean nodule field: Geology and resource potential*. Elsevier.
- Müller R. D., Royer J.-Y., Lawver L. A., 1993: Revised plate motions relative to the hotspots from combined Atlantic and Indian Ocean hotspot tracks. *Geology*, **21**, 3, 275–278, doi: 10.1130/0091-7613(1993)021<0275:RPMRTT>2.3.CO;2.
- Müller R. D., Zahirovic S., Williams S. E., Cannon J., Seton M., Bower D. J., Tetley M. G., Heine C., Le Breton E., Liu S., Russell S. H. J., Yang T., Leonard J., Gurnis M., 2019: A global plate model including lithospheric deformation along major rifts and orogens since the Triassic. *Tectonics*, **38**, 6, 1884–1907, doi: 10.1029/2018TC005462.
- Naini B. R., Leyden R., 1973: Ganges cone: A wide angle seismic reflection and refraction study. *J. Geophys. Res.*, **78**, 35, 8711–8720, doi: 10.1029/JB078i035p08711.

- Peirce J. W., 1978: The northward motion of India since the Late Cretaceous. *Geophys. J. Int.*, **52**, 2, 277–311, doi: 10.1111/j.1365-246X.1978.tb04234.x.
- Petroy D. E., Wiens D. A., 1989: Historical seismicity and implications for diffuse plate convergence in the northeast Indian Ocean. *J. Geophys. Res. Solid Earth*, **94**, B9, 12301–12319, doi: 10.1029/JB094iB09p12301.
- Rabinowitz P. D., LaBrecque J. L., 1977: The isostatic gravity anomaly: key to the evolution of the ocean-continent boundary at passive continental margins. *Earth Planet. Sci. Lett.*, **35**, 1, 145–150, doi: 10.1016/0012-821X(77)90037-1.
- Radhakrishna M., Subrahmanyam C., Damodharan T., 2010: Thin oceanic crust below Bay of Bengal was inferred from 3-D gravity interpretation. *Tectonophysics*, **493**, 1-2, 93–105, doi: 10.1016/j.tecto.2010.07.004.
- Raju D. C. V., Ravikumar S., Mishra D. C., 1998: Inversion of gravity anomaly due to a contact (fault) and its application for graben tectonics across Godavari basin. *Curr. Sci.*, **75**, 11, 1184–1188.
- Ravat D., Pignatelli A., Nicolosi I., Chiappini M., 2007: A study of spectral methods of estimating the depth to the bottom of magnetic sources from near-surface magnetic anomaly data. *Geophys. J. Int.*, **169**, 2, 421–434, doi: 10.1111/j.1365-246X.2007.03305.x.
- Ravi Kumar S., Subrahmanyam M., 2020: Deformation studies in the Central Indian Ocean, south of Sri Lanka from tentative crustal models inferred from Gravity and Magnetic data. *J. Ind. Geophys. Union*, **24**, 4, 1–19.
- Royer J. Y., Chang T., 1991: Evidence for relative motions between the Indian and Australian plates during the last 20 my from plate tectonic reconstructions: Implications for the deformation of the Indo Australian plate. *J. Geophys. Res. Solid Earth*, **96**, B7, 11779–11802, doi: 10.1029/91JB00897.
- Sandwell D. T., Müller R. D., Smith W. H. F., Garcia E., Francis R., 2014: New global marine gravity model from CryoSat-2 and Jason-1 reveals buried tectonic structure. *Science*, **346**, 6205, 65–67, doi: 10.1126/science.1258213.
- Sreejith K. M., Radhakrishna M., Krishna K. S., Majumdar T. J., 2011: Development of the negative gravity anomaly of the 85°E Ridge, northeastern Indian Ocean – A process-oriented modelling approach. *J. Earth Syst. Sci.*, **120**, 4, 605–615, doi: 10.1007/s12040-011-0099-9.
- Stein S., Okal E. A., 1978: Seismicity and tectonics of the Ninetyeast Ridge area: Evidence for internal deformation of the Indian plate. *J. Geophys. Res. Solid Earth*, **83**, B5, 2233–2245, doi: 10.1029/JB083iB05p02233.
- Stein C. A., Weissel J. K., 1990: Constraints on the Central Indian Basin thermal structure from heat flow, seismicity, and bathymetry. *Tectonophysics*, **176**, 3-4, 315–332, doi: 10.1016/0040-1951(90)90076-K.
- Straume E. O., Gaina C., Medvedev S., Hochmuth K., Gohl K., Whittaker J. M., Hopper J. R., 2019: GlobSed: Updated total sediment thickness in the world's Oceans. *Geochem. Geophys. Geosyst.*, **20**, 4, 1756–1772, doi: 10.1029/2018GC008115.
- Subrahmanyam C., Thakur N. K., Rao T. G., Khanna R., Ramana M. V., Subrahmanyam V., 1999: Tectonics of the Bay of Bengal: New insights from satellite-

- gravity and ship-borne geophysical data. *Earth Planet. Sci. Lett.*, **171**, 2, 237–251, doi: 10.1016/S0012-821X(99)00148-X.
- Subrahmanyam M., Gebissa F. T., 2017: Performance evaluation of spectral analysis and Werner deconvolution interpretation techniques in magnetic method. *J. Appl. Geophys.*, **138**, 102–113, doi: 10.1016/j.jappgeo.2017.01.017.
- Sykes L. R., 1970: Seismicity of the Indian Ocean and a possible nascent island arc between Ceylon and Australia. *J. Geophys. Res.*, **75**, 26, 5041–5055, doi: 10.1029/JB075i026p05041.
- Weissel J. K., Anderson R. N., Geller C. A., 1980: Deformation of the Indo–Australian plate. *Nature*, **287**, 5780, 284–291, doi: 10.1038/287284a0.
- Wessel P., Matthews K. J., Müller R. D., Mazzoni A., Whittaker J. M., Myhill R., Chandler M. T., 2015: Semi-Automatic Fracture Zone Tracking. *Geochem. Geophys. Geosyst.*, **16**, 2462–2472, doi: 10.1002/2015GC005853.